Shallow Reverse Moderate Earthquakes in the Weiyuan Shale Gas Field, Sichuan Basin, China, Related to Hydraulic Fracturing

Wenting Zhang[1,2,3], Rumeng Guo[*1,3,4], Lingyun Ji[2], Hongfeng Yang[5,6], Kun Dai[1], Jinping Zi[5], and Heping Sun[1,3,4]

Abstract

The Weiyuan shale gas field in the stable southern Sichuan basin, China, has experienced increasing seismicity since systematic hydraulic fracturing (HF) operations in 2015. Three $M_w \geq 4.4$ shallow earthquakes occurred in the Weiyuan area between September 2019 and February 2020, yet their seismogenic faults, rupture models, and relationship with HF are unknown. In this study, we first obtain the high-resolution coseismic deformation fields of these three events and then invert their slip distribution. The result shows that all three events are shallow high-dip reverse events under the contractional Weiyuan anticline environment with peak slips of 158, 68, and 34 cm and at depths of 4, 3, and 1.6 km, respectively. The spatial relationship between seismogenic faults, horizontal wells, as well as geological data reveals that pore-pressure diffusion due to the HF may be the main mechanism of the 8 September 2019 and the 18 December 2019 events, whereas the 16 February 2020 event may be attributed to the poroelastic stress perturbation caused by the HF. Our study highlights that HF activities and regional geological characteristics jointly influence the properties of earthquakes in the Sichuan basin.

Cite this article as Zhang, W., R. Guo, L. Ji, H. Yang, K. Dai, J. Zi, and H. Sun (2024). Shallow Reverse Moderate Earthquakes in the Weiyuan Shale Gas Field, Sichuan Basin, China, Related to Hydraulic Fracturing, *Seismol. Res. Lett.* **XX**, 1–14, doi: 10.1785/0220230375.

Supplemental Material

Introduction

The Sichuan basin is located at the northwest edge of the stable Yangtze craton, which is characterized by sedimentary layers overlying the crystalline basement. It shows a low background seismicity under a low strain rate (Lei *et al.*, 2020; Tian *et al.*, 2024). For example, fewer **M** > 4.0 earthquakes are recorded before 1970 in southern Sichuan (Dai *et al.*, 2023). Nowadays, Sichuan basin is the largest shale gas production area in China, with production primarily coming from three important shale gas production demonstration blocks: Changning, Weiyuan, and Jiaoshiba (Wang *et al.*, 2022) (Fig. 1a). The Weiyuan shale gas field is the first discovered giant gas field in China and is located in the Weiyuan–Rongxian Counties and Zizhong City, where seismic activity increased dramatically and concentrated around the horizontal wells since systematic hydraulic fracturing (HF) in 2015 (Lei *et al.*, 2020; Yi *et al.*, 2020; Zi *et al.*, 2023; Abbas *et al.*, 2024; Zhang *et al.*, 2024). The largest three earthquakes with moment magnitudes of 5.04, 4.90, and 4.39 (Yi *et al.*, 2020) occurred between September 2019 and February 2020 in the Weiyuan shale gas region, in which the M_w 5.04 event occurred on 8 September 2019, resulting in 1 death, 63 injuries, and severe damage to over 390 houses. Extensive studies based on seismological data suggested that all of them have shallow source depths and may be attributed to HF activities (Lei *et al.*, 2020; Sheng*et al.*, 2020, 2022; Wang *et al.*, 2020; Yang *et al.*, 2020; Yi *et al.*, 2020; Wong *et al.*, 2021; Liu *et al.*, 2023), yet their precise earthquake source parameters and the role of HF in fault reactivation remain unclear.

Interferometric Synthetic Aperture Radar (InSAR) has been widely employed to investigate natural earthquakes since the breakthrough study of the 1992 Landers earthquake for the advantages of high spatial resolution and positioning accuracy (Massonnet *et al.*, 1994; Elliott *et al.*, 2016), which can provide constraints for inverting slip along the fault at depth. In recent years, InSAR has been used to study the mechanism of

1. State Key Laboratory of Geodesy and Earth's Dynamic, Innovation Academy for Precision Measurement Science and Technology, Chinese Academy of Sciences, Wuhan, China, https://orcid.org/0000-0002-1799-4174 (WZ); https://orcid.org/0000-0002-5120-5335 (KD); 2. The Second Monitoring and Application Center, China Earthquake Administration, Xi'an, China; 3. College of Earth and Planetary Sciences, University of Chinese Academy of Sciences, Beijing, China; 4. Hubei Luojia Laboratory, Wuhan, China; 5. Department of Earth and Environmental Sciences, Faculty of Science, The Chinese University of Hong Kong, Shatin, Hong Kong, China, https://orcid.org/0000-0002-5925-6487 (HY); https://orcid.org/0000-0002-0891-8305 (JZ); 6. Shenzhen Research Institute, The Chinese University of Hong Kong, Shenzhen, China

*Corresponding author: guorm@asch.whigg.ac.cn

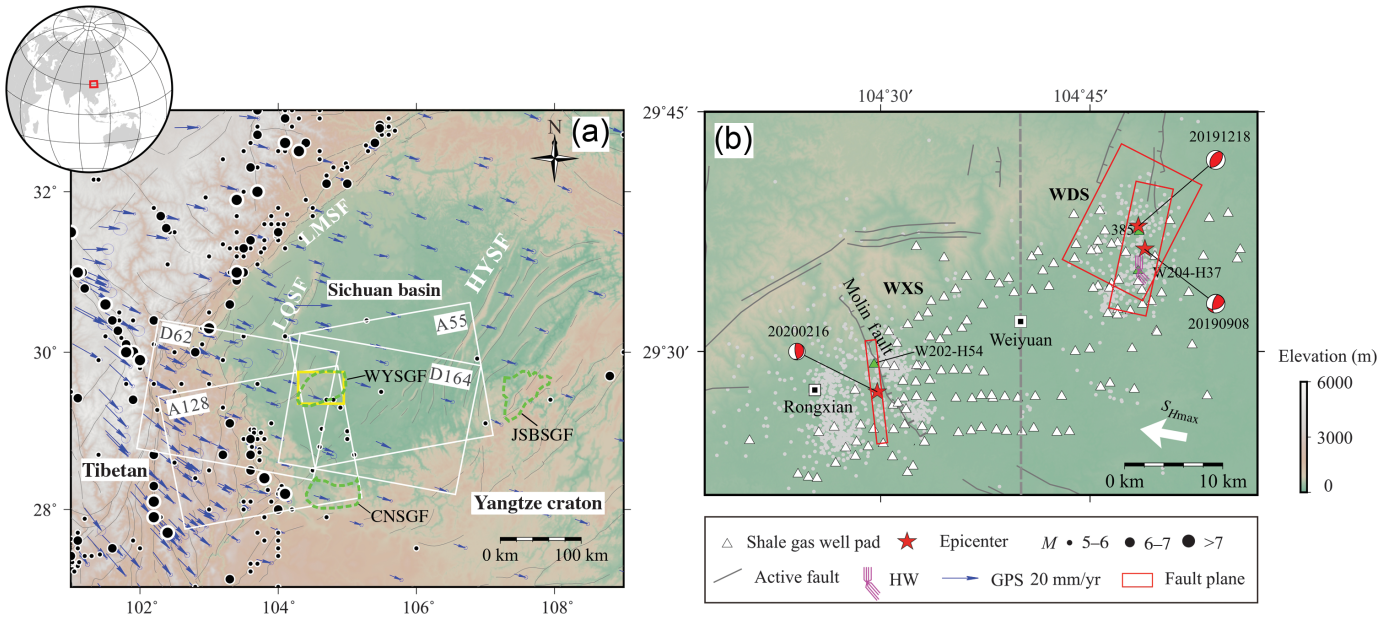

Figure 1. Tectonic setting of the Weiyuan area. (a) Satellite track images were used in this study. The green dashed polygons represent the Weiyuan (WYSGF), Changning (GNSGF), and Jiaoshiba (JSBSGF) shale gas fields. The blue arrows represent the Global Navigation Satellite Systems (GNSS) velocity field with respect to the Eurasian plate with the 95% confidence interval from Wang and Shen (2020). The gray lines represent active faults. The yellow rectangle outlines our study region. HYSF, Huayingshan fault; LMSF, Longmenshan fault; and LQSF, Longquanshan fault. The inset indicates the location of the Sichuan Basin. (b) Seismicity and hydraulic fracturing (HF) distribution in the study area. The triangles represent shale gas operation platforms, in which wells filled with green are the closest to seismogenic faults. HW indicates the horizontal well traces of the H37 horizontal well in the Weiyuan shale gas block. The gray solid circles represent relocated microearthquakes from January to March 2019 (Wang *et al.*, 2020). The red rectangles indicate fault planes used for slip distribution inversion in this study. Focal mechanisms are obtained based on our optimal slip distribution. The large white arrow manifests the orientation of the maximum horizontal principal stress ($S_{H\,max}$) (Lei *et al.*, 2020; Wang *et al.*, 2022). WDS, Weidong subblock; and WXS, Weixi subblock.

earthquakes near the HF well pad (Yang *et al.*, 2020; Eyre *et al.*, 2022; Wang *et al.*, 2022; Zhao *et al.*, 2023). In this study, we use InSAR to obtain surface deformation fields caused by the three earthquakes, then investigate the source parameters and refined slip distribution of the seismogenic faults with the constraints of InSAR observations. Finally, we discuss the induced mechanisms of the three earthquakes by combining the regional geological background and analyzing the spatial relationship between the coseismic slip distribution and the HF well.

Geological Setting and Seismicity in the Weiyuan Shale Gas Field

The Weiyuan shale gas field is located in the southern large dome contractional anticline of the stable Sichuan basin, with the Longquan Mountain structural belt in the west, the central Sichuan monocline in the north, and the Zigong sag in the south (Wei *et al.*, 2008; Wang, Hubbard, *et al.*, 2016). The azimuth of the maximum principal stress based on earthquake focal mechanisms is 106° (Lei *et al.*, 2020), which is consistent with the direction of the Global Positioning System velocity field in the area (Fig. 1a) (Wang *et al.*, 2020). Rich shale gas reservoirs have been explored in the Upper Ordovician Wufeng Formation (O_3W)–Lower Silurian Longmaxi Formation (S1l) of the Weiyuan shale gas field (Zou *et al.*, 2015), which is characterized by large shale thickness, high gas content, developed fractures, and weak stress heterogeneity (Liu and Wang, 2016). The burial depth of the reservoirs is about 1.2–3.5 km from the western to the eastern part (Zou *et al.*, 2020).

The Weiyuan shale gas field can be divided into the Weixi subblock in the west and the Weidong subblock in the east, with the boundary line roughly passing through Weiyuan County (Lei *et al.*, 2020; Yang *et al.*, 2020) (Fig. 1b). In the Weidong subblock, a large number of small earthquakes occurred in the first four years after the large-scale HF in 2015. The largest event magnitude was 3.6 until the M_w 5.04 earthquake occurred on 8 September 2019, and another M_w 4.90 earthquake occurred ~4 km northeast of it on 18 December 2019. Seismological data show similar reverse focal mechanisms of these two earthquakes, and the nearby W204-H37 platform experienced fracking before the M_w 5.04 event (Zi *et al.*, 2023). The Weixi subblock also hosts a series of earthquakes with $M_w \geq 4$. On 24 and 25 February 2019, three moderate earthquakes occurred in the Molin area, which may be attributed to HF by analyzing the spatiotemporal relationship between earthquakes and HF activities (Lei *et al.*, 2020; Yang *et al.*, 2020). The largest M_w 4.30 event is interpreted to occur on the shallow Molin fault with

a limited extending depth of ~1.5 km (Wang *et al.*, 2020; Yang *et al.*, 2020). Tomography results further reveal the existence of a low-velocity zone extending ~4 km along the Molin fault, which is supposed to be geologically susceptible and prone to occurring $M_L \geq 3.0$ earthquakes (Zi *et al.*, 2023). Around 1 yr later (16 February 2020), another M_w 4.39 event occurred in the same area (Yi *et al.*, 2020), but detailed research has not yet been conducted.

InSAR Observations

InSAR data processing

It is challenging to study small-to-moderate earthquakes (i.e., $M_w < 5.5$) with Differential InSAR (DInSAR) because their surface deformation is usually small and likely to be contaminated by atmospheric delays or low coherence (Luo *et al.*, 2022). Thus, we apply the multi-interferogram stacking method to estimate the average differential phase with an improved signal-to-noise ratio using a set of unwrapped differential interferograms under the assumption of randomly distributed atmospheric delays and constant deformation (Jiang *et al.*, 2018; Luo *et al.*, 2022; Wang *et al.*, 2022; Zhao *et al.*, 2023).

Sentinel-1 satellite SAR images from ascending tracks T55A and T128A and descending tracks T62D and T164D captured the coseismic deformation associated with the 8 September 2019, 18 December 2019, and 16 February 2020 events (Fig. 1a). The GAMMA commercial software platform is utilized to process the SLC images (Werner *et al.*, 2000). The enhanced spectral diversity method (Yagüe-Martínez *et al.*, 2016) is used to improve the coregistration accuracy. We generate interferograms spanning the earthquake with temporal baselines smaller than 60 days for stacking. Topographic contributions to the interferograms are simulated and subtracted based on the 30 m spatial resolution SRTMGL1 DEM. In addition, a multilook factor of 10:2 and the weighted power spectrum filter (Goldstein and Werner, 1998) are applied to improve the coherence. The minimum cost flow algorithm (Costantini, 1998) is conducted for unwrapping, and reference points are selected at stable points away from deformation areas. We use the Generic Atmospheric Correction Online Service for the InSAR online weather model to estimate and mitigate the atmospheric phase delays (Yu *et al.*, 2018), then use the linear polynomial to fit and remove regular stripes caused by residual long-wave effects based on data away from deformation areas. We further discard interferograms severely affected by atmospheric phase delays, decorrelation, or unwrapping errors and finally obtain a series of refined interferograms spanning the three earthquakes. The baseline maps of the retained interferograms are shown in Figure S1, and detailed interferogram information for each track is listed in Table S1, available in the supplemental material to this article. Notably, not all four tracks are involved in the interferogram selection of the 8 September 2019 and 18 December 2019 events. Subsequently, we conduct the multi-interferogram stacking method based on the selected interferograms to obtain the stacked phases and convert them to obtain three coseismic deformation fields along the line-of-sight (LoS) direction in the local World Geodetic System 1984 (WGS 84) coordinate system with a 30 m resolution (Fig. 2).

To evaluate the effectiveness of the multi-interferogram stacking method, we estimate the standard deviation of the initial DInSAR deformation fields as well as the stacked deformation fields by masking out the area of coseismic deformation. The result shows that for the 8 September 2019 event, the standard deviations of the stacked deformation fields for T55A and T164D are 0.4 and 0.4 cm, respectively. For the event on 18 December 2019, the standard deviations of the stacked deformation fields for T55A, T128A, and T164D are 0.3, 0.2, and 0.3 cm, respectively. For the event 20200216, the standard deviations of the stacked deformation fields for the T55A, T128A, T164D, and T62D are 0.2, 0.2, 0.1, and 0.2 cm, respectively. Details on the standard deviation of the initial DInSAR results are listed in Table S1. We also estimate the mean values of the stacked deformation fields utilizing values within the coseismic deformation area. The result shows that for the 8 September 2019 event, the mean values of the stacked deformation fields for T55A and T164D are 1.1 and 1.5 cm, respectively. For the 18 December 2019 event, the mean values of the stacked deformation fields for the T55A, T128A, and T164D are 1.1, 0.7, and 0.7 cm, respectively. For the 16 February 2020 event, the mean values of the stacked deformation fields for the T55A, T128A, T164D, and T62D are 1.0, 0.7, 0.4, and 0.4 cm, respectively.

Coseismic interferograms

Figure 2 shows the stacked coseismic deformation fields of the three events. It can be seen that for each event, both ascending and descending observations have the same positive and negative characteristics. According to radar geometric parameters, this consistency of deformation direction under different LoS directions indicates that the coseismic deformation is dominated by vertical motions. Warm colors represent motions close to the satellite, and cold colors represent motions away from the satellite, manifesting all these three events are dominated by reverse components, consistent with previous seismological estimations (Lei *et al.*, 2020; Sheng *et al.*, 2020; Wang *et al.*, 2020; Yi *et al.*, 2020). For the 8 September 2019 event, the maximum deformation values for T55A and T164D in the LoS direction are 2.8 and 2.9 cm, respectively. For the 18 December 2019 event, the maximum deformation values for T55, T128A, and T164D in the LoS direction are 2.2, 1.6, and 1.5 cm, respectively. For the 16 February 2020 event, the maximum deformation values for T55A, T128A, T62D, and T164D in the LoS direction are 1.8, 1.6, 0.8, and 1.0 cm, respectively.

Interferogram down-sampling

To improve the efficiency of slip inversion, we need to down-sample the coseismic displacements. However, the commonly used quadtree down-sampling method is sensitive not only to

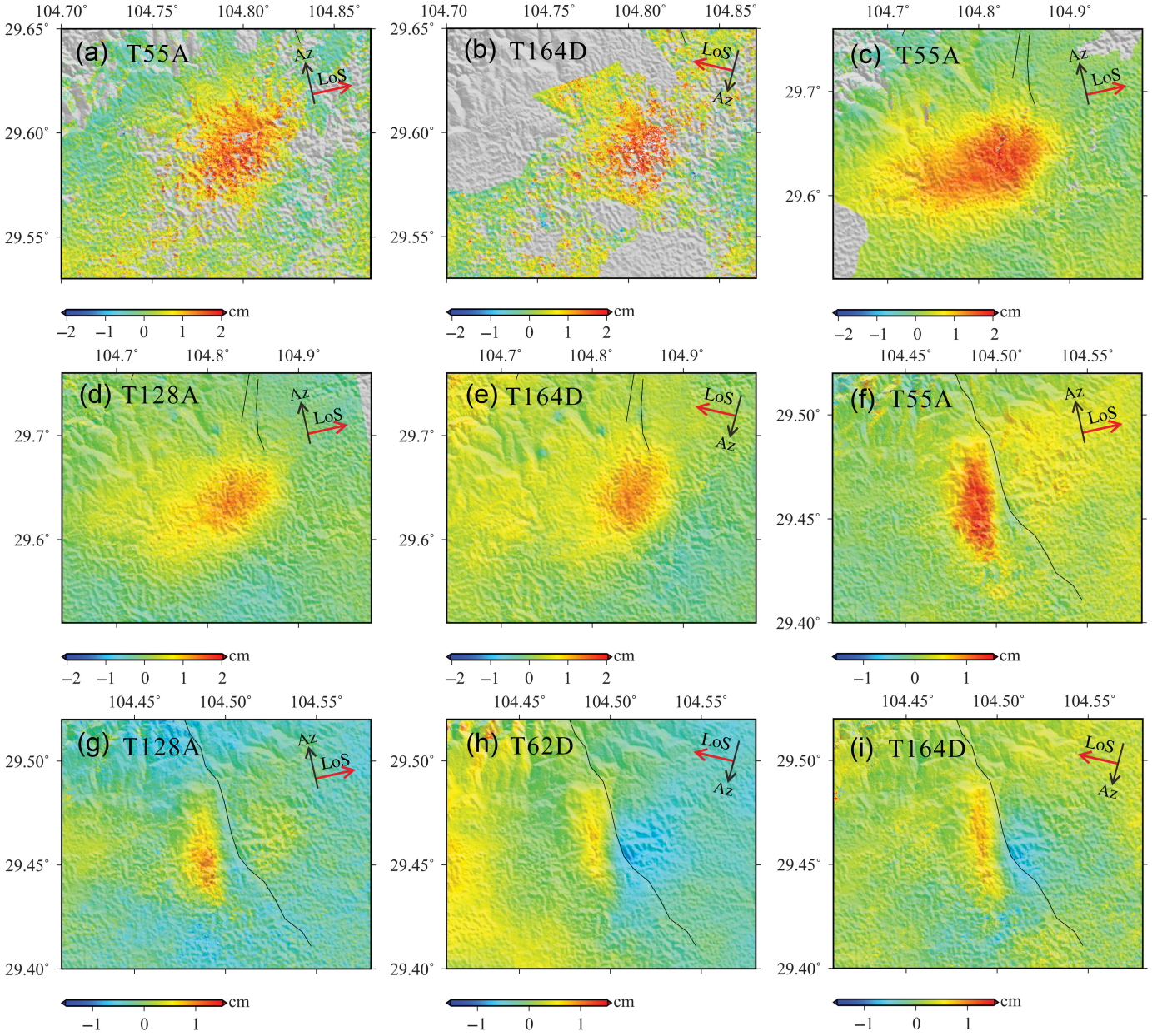

Figure 2. Coseismic deformation from different tracks associated with the (a,b) 8 September 2019, (c–e) 18 December 2019, and (f–i) 16 February 2020 events. Positive values indicate motions close to the satellite, and negative values indicate motions away from the satellite. The gray lines represent active faults.

deformation but also to phase gradients caused by noises like atmosphere phases and incoherence (Ji *et al.*, 2017; Luo *et al.*, 2022). This phenomenon is more pronounced when sampling deformation from small to moderate earthquakes since the magnitude of errors is close to the magnitude of deformation. Therefore, we apply a uniform grid sampling method based on topology analysis to mitigate unreasonable oversampling in the far-field regions (Wang *et al.*, 2022). The method first constructs a polygon based on the distribution of each coseismic deformation and then down-samples the deformation field with different grids inside and outside the polygon. We down-sample all deformation fields with intervals of 0.0035° inside the polygon and 0.015° outside the polygon by trading off the number and density of sampling points. For the 8 September 2019 event, we obtain 1008 and 1753 observations for T55A and T164D, respectively. For the 18 December 2019 event, we obtain 1436, 1553, and 1479 observations for T55A, T128A, and T164D, respectively. For the 16 February 2020 event, we obtain 716, 718, 717, and 718 observations for T55A, T128A, T62D, and T164D, respectively.

Fault Source Modeling

To investigate whether and how HF induced these earthquakes, we need to invert the detailed source parameters and slip distribution with the constraints of high-resolution

InSAR observations. We first perform a nonlinear inversion to search for the best-fit fault source parameters, then conduct a linear inversion based on the steepest descent method (SDM) program (Wang *et al.*, 2013) to obtain the refined slip distribution.

Determination of source model parameters

To determine the optimal source parameters, we use the nonlinear Bayesian approach to invert InSAR observations obtained from different paths, which allows a rapid calculation of posterior probability density functions of source model parameters using a Markov chain Monte Carlo method (MCMC) and the Metropolis–Hastings algorithm (Bagnardi and Hooper, 2018). We perform the inversion with a rectangular dislocation source (Okada, 1985) using nine source model parameters: length, width, depth of the lower edge, dip, strike, uniform slip along strike and dip direction, and X and Y coordinates of the midpoint of the lower edge. During the inversion, we set the range of dip and strike between 0°–90° and 0°–360° for global search and randomly choose the initial parameters within the ranges.

The marginal posterior probability distribution for the source model parameters of the three events is shown in Figure 3, with the maximum posterior probability solutions and the 95% credible intervals as follows. For the 8 September 2019 event, our preferred model reveals that the coseismic deformation can be well explained by uniform slip on a 4498 (−4027/+2594)-m-long and 1306 (−278/+3216)-m-width fault with a centroid depth of 3563 (−444/+2460) m, striking 192° (−12.5°/+21°), dipping 64° (−9.8°/+9.5°) (fault 1), and the optimal strike-slip and reverse slip are −0.32 (−0.6/+0.24) m and 0.14 (−0.1/+0.75) m, respectively. For the 18 December 2019 event, the result reveals that coseismic surface displacements can be well explained by uniform slip on a 4291 (−1452/+1114)-m-long and 7463 (−4614/+294)-m-width fault with a centroid depth of 4488 (−2059/+769) m, striking 207° (−10°/+14°), dipping 46° (−6°/+12°) (fault 2), and the optimal strike-slip and reverse slip are 0.03 (−0.01/+0.04) m and 0.04 (−0.01/+0.06) m, respectively. For the 16 February 2020 event, our model result reveals that coseismic surface displacements can be well explained by slip on a 5067 (−509/+493) m long and 210 (−6/+750) m wide fault, striking 174° (−2.3°/+1.7°), dipping 72° (−5.4°/+5.2°) (fault 3) with a centroid depth of 1667 (−80/+422) m, and the optimal strike-slip and reverse slip are −0.04 (−0.09/+0.14) m and 0.3 (−0.2/+0.02) m, respectively.

Static finite-fault inversion

Based on the fault parameters obtained earlier, we further investigate the refined slip distribution of the seismogenic fault planes. To prevent possible boundary effects, we extend fault 1 obtained in 4.1 by increasing the length to 15 km and the down-dip width to 10 km. Similarly, faults 2 and 3 are extended by increasing the length to 15 and 12 km and increasing the down-dip width to 30 and 4 km, respectively. All fault planes are set to reach the ground surface to capture possible shallow slips. We discretize all fault planes into rectangular patches with a mesh of 0.5 × 0.5 km to obtain 600, 900, and 192 patches for faults 1, 2, and 3, respectively. Before the inversion, we first compute Green's functions based on the elastic half-space dislocation model. And then, the down-sampled InSAR data are inverted to obtain the coseismic slip based on the SDM program (Wang *et al.*, 2013), which is implemented on the constrained least-squares method. We apply the L-curve method to select the smoothing factors between the model roughness and data misfit (Hansen, 1999). As shown in Figure S2, our preferred smoothing parameters are 0.03, 0.02, and 0.03 for faults 1, 2, and 3, respectively.

Results

The 8 September 2019 event

A comparison of observations and predictions associated with the coseismic LoS displacements along T55A and T164D is shown in Figure 4. It can be seen that the model can fit all observations well. The geodetic moment is about 4.21×10^{16} N · m, which is equivalent to an M_w 5.05 event, comparable to the seismological estimation from Yi *et al.* (2020) (M_w 5.04), smaller than the result estimated by Wang *et al.* (2020) (M_w 5.20), and slightly larger than the results estimated by Lei *et al.* (2020) (M_w 4.92) and Sheng *et al.* (2020) (M_w 4.97). There is no surface rupture, and most of the slip is concentrated on a ∼4 × 4 km region, passing through the Wufeng–Longmaxi formation shale gas bed (3.1–3.5 km) (Dong *et al.*, 2018), and the maximum slip is 158 cm at the depth of ∼4 km. The slip asperity is dominated by significant reverse and minor sinistral components, closing to the fluid injection depth of the horizontal well W204-H37. In addition, we calculate shear stress change on the source fault triggered by the 8 September 2019 event with a static frictional coefficient of 0.6 and a rigidity of 30 GPa, respectively (Guo *et al.*, 2020). As shown in Figure 4i, the maximum shear stress change is located near the epicenter with a magnitude of 0.92 MPa.

The 18 December 2019 event

As shown in Figure 5, the coseismic LoS displacements along T55A, T128A, and T164D of the 18 December 2019 event are well recovered. The geodetic moment is about 5.74×10^{16} N · m, corresponding to an M_w 5.14 event, which is slightly larger than the seismological results (Lei *et al.*, 2020; Sheng *et al.*, 2020; Yi *et al.*, 2020). Our model reveals that most of the slip is concentrated on an area of ∼5.5 × 5.0 km without the surface rupture, passing through the Wufeng–Longmaxi formation shale gas bed (3.1–3.5 km), and the maximum slip is 68 cm at the depth of ∼3 km (Dong *et al.*, 2018), near the fracking injection depth of the horizontal well 385. The slip asperity is dominated by significant thrust and minor sinistral components, generally consistent with the result of seismological estimations. Except for the main slip asperity, we find a small amount of slip with a depth range

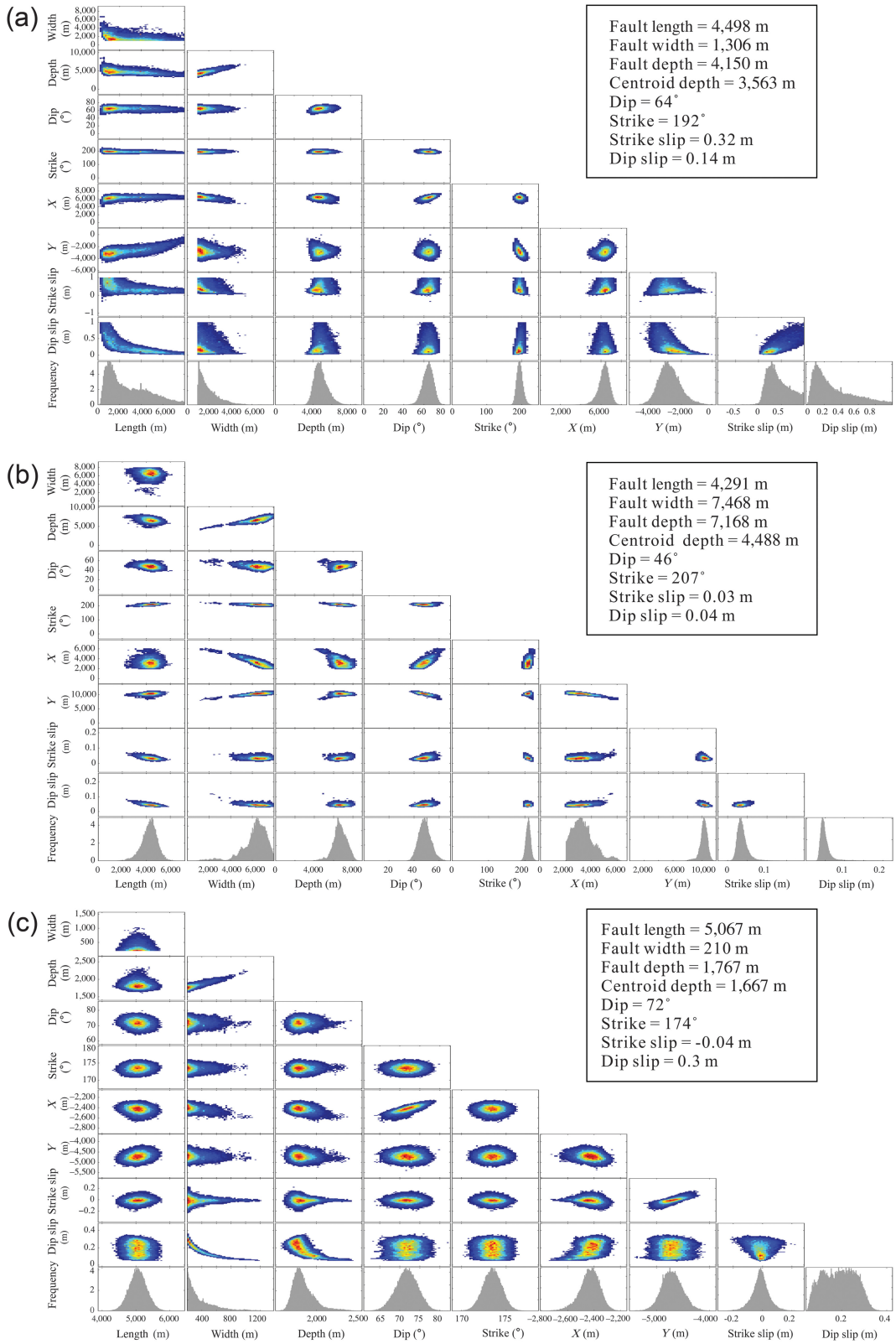

Figure 3. The marginal posterior probability distribution for the source model parameters of the (a) 8 September 2019, (b) 18 December 2019, and (c) 16 February 2020 events. Scatter plots are contoured based on frequency (warm colors represent high frequency, cold colors represent low frequency). Optimal parameters are labeled in the insets.

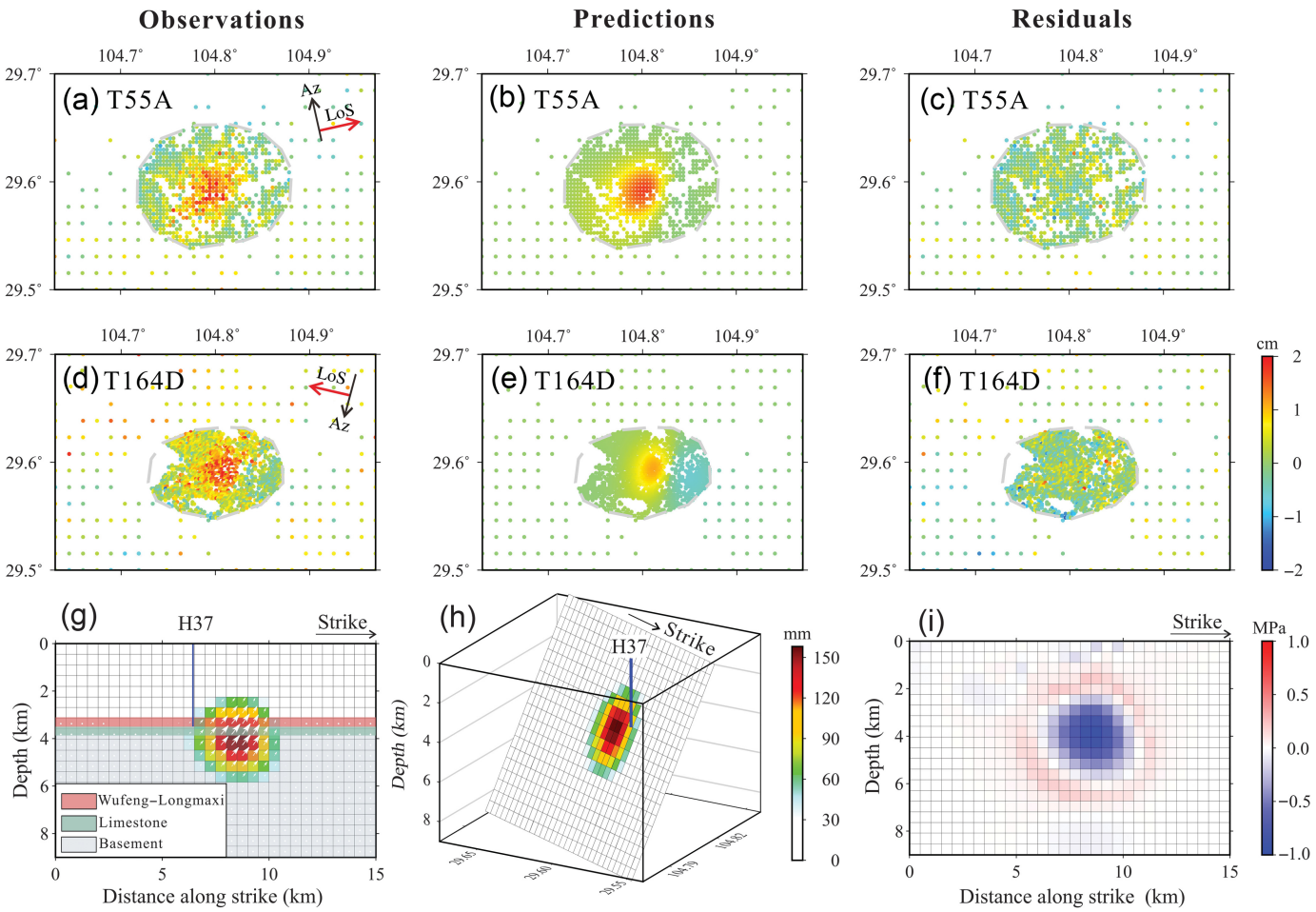

between 4 and 8 km, resulting in a larger seismic moment. The maximum shear stress change (Fig. 5i) triggered by the 18 December 2019 event is located near the epicenter with a magnitude of 0.35 MPa, smaller than that of the 8 September 2019 event.

The 16 February 2020 event

Figure 6 demonstrates that comparison of observations and predictions of the coseismic LoS displacements associated with the 16 February 2020 event along T55A, T128A, T62D, and T164D, revealing a good fit. The geodetic moment is about 8.6×10^{15} N · m, corresponding to an M_w 4.59 event, which is slightly larger than the seismological estimation from Yi *et al.* (2020) (M_w 4.39). Our optimal slip distribution suggests that most of the slip is concentrated on a ~6.5 × 2.5 km region, where the maximum slip is 34 cm at a depth of ~1.6 km, shallower than the depth of the shale gas bed in this area (2.45–2.7 km) (Dong *et al.*, 2018). The slip asperity is dominated by significant reverse and minor strike-slip components, generally consistent with the result of seismological estimations. Meanwhile, the shear stress change on the source fault triggered by the 16 February 2020 event shows that the maximum shear stress is located near the epicenter with a magnitude of 0.26 MPa (Fig. 6i), smaller than that of the 8 September 2019 and 18 December 2019 events.

Figure 4. Comparison of observations and predictions derived from our optimal slip distribution associated with the 8 September 2019 event along tracks (a–c) T55A and (d–f) T164D, respectively. (g) 2D and (h) 3D coseismic slip distribution. The white arrows indicate the slip directions, and the blue lines represent the location of the nearest well pad. (i) Shear stress perturbation triggered by the 8 September 2019 event.

Equivalent nodal planes from InSAR

Based on our preferred slip models of the 8 September 2019, 18 December 2019, and 16 February 2020 earthquakes, we estimate their equivalent focal mechanisms by assuming an average shear modulus G = 30 GPa and calculating the total moment tensors of each slip distribution grid (Guo *et al.*, 2023). The focal mechanisms (strike/dip/rake) of the 8 September 2019, 18 December 2019, and 16 February 2020 events are 192°/64°/54°, 207°/46°/80°, and 173°/72°/78°, respectively. For further comparison with seismological results, we calculate the Kagan angles (Kagan, 1991) between the focal mechanisms from our InSAR observations and previous studies (Table 1). It can be seen that for the 8 September 2019 event, the Kagan angle varies from 19.4° to 55.2°; for the 18 December 2019 event, the Kagan angle varies from 6.5° to 20.3°; and for the 16 February 2020 event, the Kagan angle is 13.8°. Thus, we argue that for the 18 December

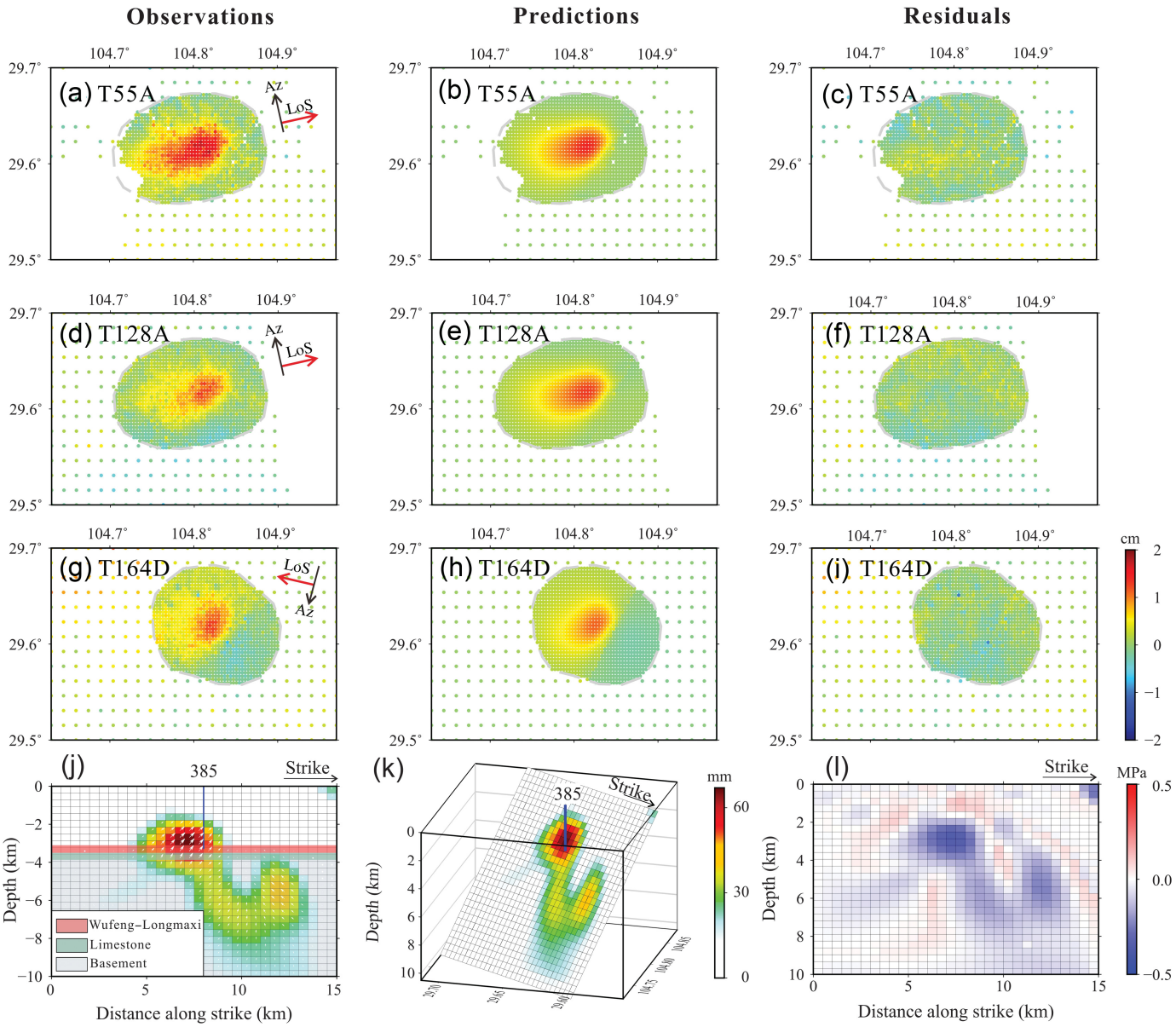

Figure 5. Comparison of observations and predictions derived from our optimal slip distribution associated with the 18 December 2019 event along the (a–c) T55A, (d–f) T128A, and (g–i) T164D, respectively. (j) 2D and (k) 3D coseismic slip distribution. (l) Shear stress perturbation triggered by the 18 December 2019 event. Other symbols are the same as in Figure 4.

2019 and the 16 February 2020 events, the geodetic and seismological source parameters are similar, whereas for the 8 September 2019 event, there are larger differences between the geodetic and the seismology results. In addition, the focal mechanism of the 16 February 2020 event is similar to the M_w 4.30 event that occurred in the same area on 25 February 2019 (Wang *et al.*, 2020; Yang *et al.*, 2020).

Discussion

Shallow reverse destructive earthquakes in the Weiyuan shale gas field

In this study, we determine the detailed source parameters and slip distribution of three moderate earthquakes in the Weiyuan shale gas field that occurred between September 2019 and February 2020. The 8 September 2019 and 18 December 2019 events occurred on previously unmapped reverse faults, and the 16 February 2020 event may occur on the reverse Molin fault (Fig. 1b). All these three earthquakes are striking approximately along the north–south direction and the P axis of the earthquake focal mechanisms is generally consistent with the regional tectonic stress orientation (Fig. 1b), indicating that the seismogenic faults are optimally oriented relative to the regional stress field and can be readily reactivated. Compared with the Changning shale gas field characterized by both strike- and reverse-slip events, the unified reverse events in the Weiyuan field indicate a more simple stress environment (Lei *et al.*, 2020; Wang *et al.*, 2022).

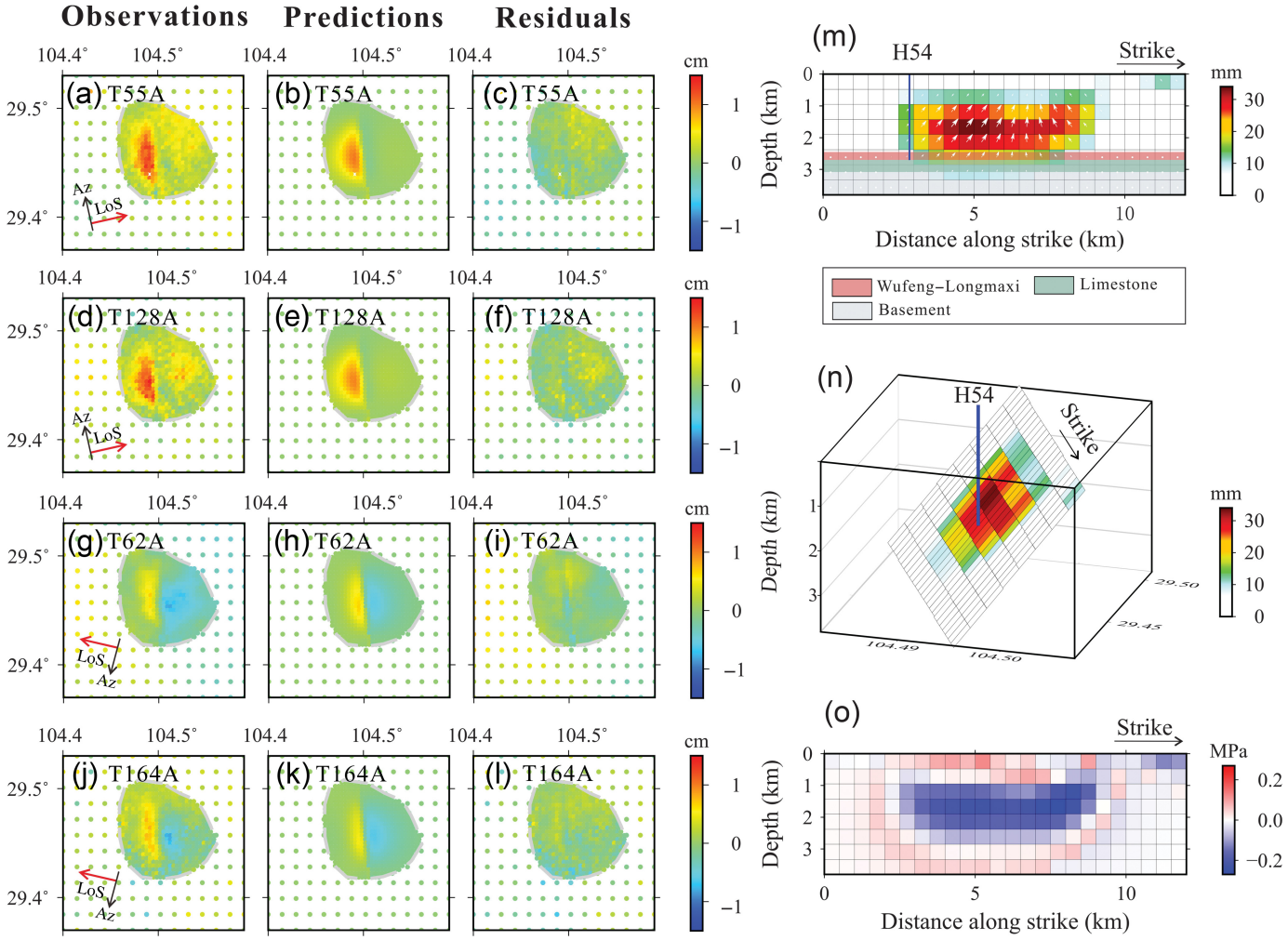

Figure 6. Comparison of observations and predictions derived from our optimal slip distribution associated with the 16 February 2020 event along the (a–c) T55A, (d–f) T128A, (g–i) T62D, and (j–l) T164D, respectively. (m) 2D and (n) 3D coseismic slip distribution. (o) Shear stress perturbation triggered by the 16 February 2020 event. Other symbols are the same as in Figure 4.

Different from HF-induced earthquakes in western Canada and the United States for which hypocenters are proximal to the basement (Bao and Eaton, 2016), these three earthquakes in the Weiyuan shale gas field occurred above the crystalline basement. Particularly, the 16 February 2020 event in the Weixi subblock occurred at an extremely shallow depth (<2 km), which challenges the traditional view that the shallow crust (<2 km) exhibits velocity-strengthening behavior and the expectation of laboratory friction experiments on sedimentary rock samples for slip aseismically (Verberne *et al.*, 2010). One possible explanation is that this area used to receive tectonic denudation for ~4 km (Liu *et al.*, 2021). The rocks in shallow depths nowadays may be previously buried deeply and exhibit different frictional properties. In addition, HF-induced earthquakes in the Weiyuan shale gas field are characterized by high-dip reverse faults with dip angles of ~46°–72°, which manifests the reactivation of high-dip pre-existing faults in the WYGSF.

Mechanisms of induced earthquakes

Three mechanisms are widely recognized to explain HF-induced earthquakes (Ellsworth, 2013; Eyre *et al.*, 2019; Schultz *et al.*, 2020; Wang *et al.*, 2020). The first mechanism is a pore-pressure perturbation, which can decrease the effective normal stress on the pre-existing fault and weaken the fault zone directly connected to the hydraulic fractures through elevated fluid pressures. The second mechanism is poroelastic stress transfer, which can change the loading conditions on a fault plane without a direct hydraulic connection. The third one is injection-induced aseismic slip, which could cause dynamic rupture when the deformation front impinges on distal unstable regions of the fault. Compared with the first two mechanisms, the third mechanism can stimulate earthquakes in shorter injection timescales and far from the injection point. Therefore, we can speculate potential mechanisms of the induced earthquakes by combining and analyzing the spatial and temporal relationship between the earthquakes and the HF activities. In this study, we first project the inverted slip distribution and the nearest fracking wells of these three earthquakes along profiles across their epicenters on the

TABLE 1
Source Parameters of the Three Earthquakes in the Weiyuan Area

Event	Epicenter		Depth (km)	Nodal plane Ⅰ (°)			Nodal plane Ⅱ (°)			Magnitude			Focal mechanism	Kagan Angle (°)	Source
	E (°)	N (°)		strike	dip	rake	strike	dip	rake	Mw	Ms	M_L			
20190908	104.79	29.55	10	-	-	-	-	-	-	-	5.40	-	-	-	CENC
	105.064	29.573	11.5	19	46	59	240	52	118	5.04	-	-		55.2	USGS
	104.89	29.55	12	40	30	103	205	61	83	5.10	5.00			25.1	GCMT
	104.815	29.607	3.56	-	-	-	192	64	54	5.05	-	-		-	a
	104.805	29.5796	4.5	40	32	94	215	58	87	5.04	5.40	5.60		30.1	b
	104.82	29.58	2.48	25	39	70	230	54	105	4.92	5.40	-		45.3	c
	104.812	29.602	2.9	57	26	123	201	68	75	4.97		5.40		19.4	d
	104.931	29.53	5	-	-	-	-	-	-	5.20	-	-	-	-	e
20191218	104.82	29.59	-	-	-	-	-	-	-	-	5.20	-	-	-	CENC
	104.946	29.639	11.5	48	49	105	205	43	73	4.87	-	-		6.5	USGS
	104.86	29.52	12	51	33	123	193	63	71	4.90	4.90	-		20.3	GCMT
	104.808	29.631	4.49	-	-	-	207	46	80	5.14	-	-		-	a
	104.8283	29.6383	4	35	29	94	210	61	88	4.90	5.20	5.40		16.4	b
	104.82	29.59	2.54	20	41	71	225	52	106	4.73	5.20	-		20.0	c
	104.88	29.642	2.9	47	28	110	205	64	80	4.78	-	5.20		18.1	d
20200216	104.5	29.48	10	-	-	-	-	-	-	-	4.40	-	-	-	CENC
	104.496	29.458	1.67	174	72	78	-	-	-	4.59	-	-		-	a
	104.4833	29.4833	2.5	0	29	99	170	61	85	4.39	4.40	4.70		13.8	b

The depths of this study refer to the maximum slip depth from linear inversion. CENC, China Earthquake Networks Center (see Data and Resources); Global CMT, Global Centroid Moment Tensor (see Data and Resources); and USGS, U.S. Geological Survey (see Data and Resources); a. This study; b. Yi *et al.* (2020); c. Lei *et al.* (2020); d. Sheng *et al.* (2020); e. Wang *et al.* (2020).

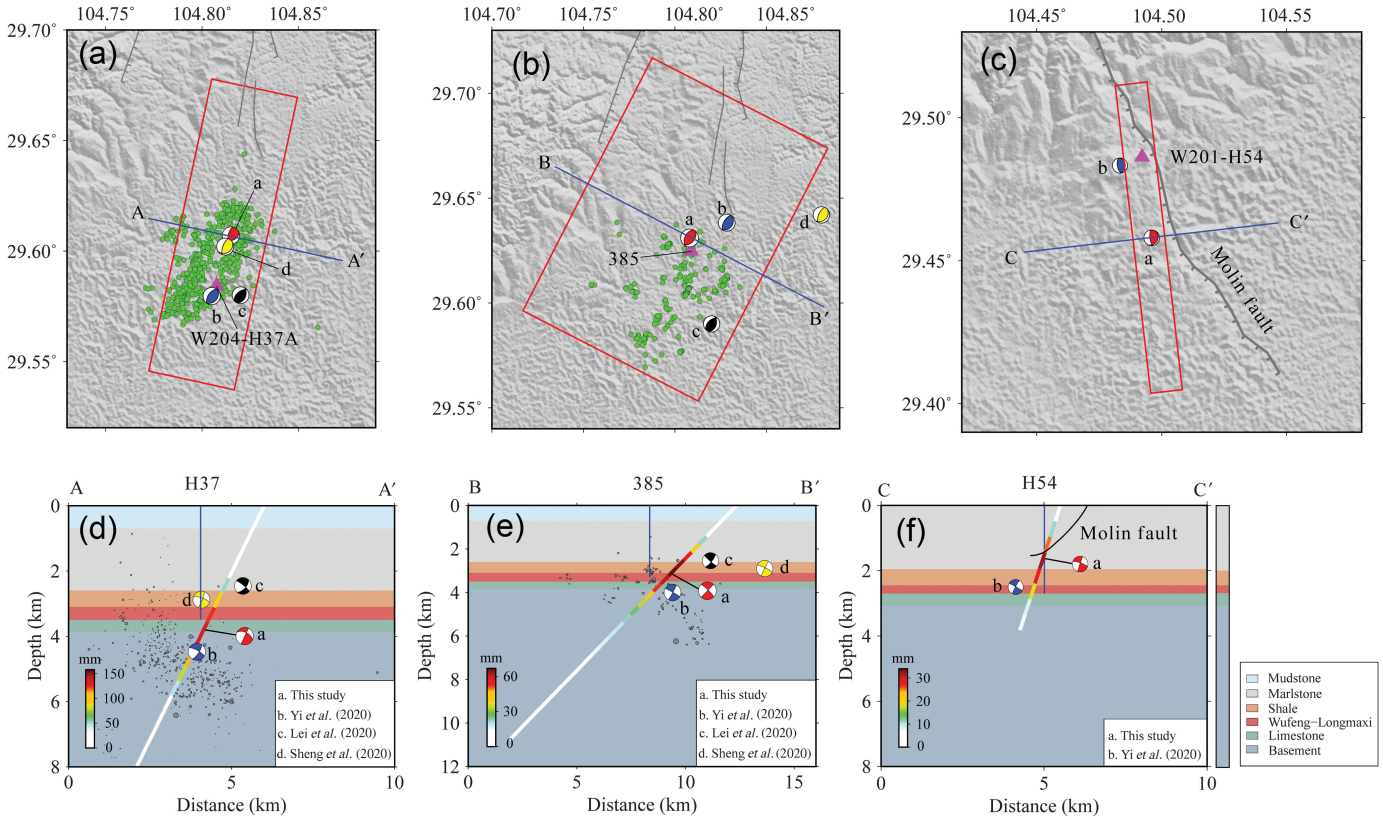

Figure 7. Maps and section views. (a) Fault planes, focal mechanisms from different studies, aftershocks, and the nearest fracking wells. Slip distribution, moment tensor solutions, seismicity, the nearest fracking wells, and the Molin fault are projected on the cross-section of (b) AA′, (c) BB′, and (d) CC′. The simplified geological sections (Dong *et al.*, 2018) are represented using different colors.

simplified geological sections (Dong *et al.*, 2018) to clarify their spatial relationship (Fig. 7). Subsequently, we discuss the potential mechanisms of the three earthquakes by combining the regional geological background and analyzing the hydraulic connectivity between the seismogenic faults and the fluid injection point (Ellsworth, 2013).

For the 8 September 2019 and 18 December 2019 events, our results show that the high-slip regions are very close to the fluid injection points (several hundred meters) in the Wufeng–Longmaxi formation (Fig. 7d,e), indicating that pore-pressure perturbation caused by the fracking fluid injection could be transferred to the nearby pre-existing faults. HF operations could create and extend fractures, forming potentially conductive channels for pore-pressure diffusion (e.g., Wang *et al.*, 2022). In general, the high-dip reverse faults are difficult to slip, and high pore pressure is required to activate them (Eyre *et al.*, 2019; Chu and Sheng, 2023). Thus, we argue that the 8 September 2019 and 18 December 2019 events may be attributed to the pore-pressure diffusion caused by the pressurized fluids. Notably, the 8 September 2019 event imposed positive stresses in the 18 December 2019 earthquake source region (Sheng *et al.*, 2020), pushing the seismogenic fault into a stress-critical state and thus susceptible to activation after fluid injection. Figure 7d,e shows that the distribution of aftershocks is not coincidental with our optimal fault planes, indicating that the fault system in this region may be more complex.

For the 16 February 2020 event, the maximum slip inverted from InSAR data is located at the Marlstone layer (~1.6 km) and in proximity to the bottom of the Molin fault interpreted from seismic reflection profiles (Wang *et al.*, 2020) (Fig. 7f), indicating that the Molin fault may be the seismogenic fault. However, the fluid injection depth of the nearest W202-H54 horizontal well is located in the Wufeng–Longmaxi formation (2.45-2.7 km) (Fig. 7f), significantly larger than the focal depth of the mainshock. Note that the ~800 m thickness shale layer atop the Wufeng–Longmaxi formation is characterized by low permeability and porosity. Such that the injected fluid is more likely to significantly decrease overburden pressure, promoting reverse-faulting ruptures. Meanwhile, because it reveals that the seismogenic Molin fault should not hydraulically connect with the injection point, the pore-pressure perturbation should not be the main mechanism attributed to the reactivation of the Molin fault. In addition, because the seismogenic Molin fault has a limited extending depth of ~1.5 km on the overlying Marlstone and away from the injection point, it is less likely that the event was stimulated by injection-induced aseismic slip. Thus, we infer that the 16 February 2020 event is likely to be related to stress changes arising from poroelastic coupling

between hydraulic fractures and the rock matrix, which can alter fault-loading conditions without any hydraulic connection and has been suggested to impact fault in distance (Segall and Lu, 2015; Deng *et al.*, 2016; Goebel and Brodsky, 2018). A similar mechanism has been found in the 25 February 2019 M_w 4.30 earthquake in the same area (Yang *et al.*, 2020). Although there is debate about whether poroelastic stresses alone can predominantly influence the process of induced earthquakes (Zhai *et al.*, 2021), our study suggests that the far-field triggering of poroelastic stress could cause **M** > 4 earthquakes in the Weiyuan shale gas field. Notably, due to the lack of industrial data, we cannot estimate the crustal stress perturbations and completely rule out other mechanisms.

Conditions of induced earthquakes in the Sichuan basin

Induced earthquakes are generally caused by the reactivation of existing faults with characteristics of small relative displacement, low maturity, and being in a subcritical stress state (Lei *et al.*, 2014). For example, the occurrence of a fault appropriately oriented for slip under a given stress field near the injection or production wells. However, the mechanisms of induced seismicity in the Sichuan basin vary in different regions. For the three demonstration blocks, the Changning block exhibits the most induced seismicity, whereas the Jiaoshiba block exhibits the least induced seismicity (Lei *et al.*, 2020; Wang *et al.*, 2022). These distinct responses could be attributed to the differences in density and scale of pre-existing faults, injection pressure, orientation of faults (Lei *et al.*, 2020), in situ stress (Wang, Huang, *et al.*, 2016), as well as strain rate (Wang *et al.*, 2022).

Considering the widely developed small and immature faults within the brittle formations in the Sichuan basin, it is crucial to evaluate potential seismic hazards induced by HF activities. Given the complex mechanisms and conditions of the induced earthquakes, we should monitor the entire shale gas production process by comprehensively using geodetic and seismological methods with high temporal and spatial resolution. In addition, buried faults in the basement may exhibit different seismic responses to injection activities (Kozłowska *et al.*, 2018), reminding us not to ignore the risks of deeper seismic activities.

Conclusion

Understanding the mechanism of fundamental processes of fault reactivation during HF is critical for mitigating seismic hazards. In this study, we obtain the coseismic InSAR deformation fields of three $M_w \geq 4.4$ earthquakes in the Weiyuan shale gas field in China and invert their slip distribution. Our model results show that all three earthquakes are characterized by shallow reverse asperity with high-dip angles. The spatial relationship between fault planes and HF wells implies that both pore-pressure diffusion and poroelastic stress transfer can become the dominant inducing mechanisms of earthquakes in the Weiyuan shale gas field. A comparison of seismic activity in different blocks indicates that HF activities and regional geological characteristics jointly influence the properties of induced earthquakes in the Sichuan basin. This study highlights that it is paramount for us to continuously monitor the deformation and seismicity activity with high accuracy for the assessment of seismic hazards and sustainable development of the shale gas industry.

Data and Resources

The Sentinel-1 Synthetic Aperture Radar (SAR) images are provided free by European Space Agency's (ESA) Sentinels Scientific Data Hub (https://scihub.copernicus.eu/). The focal mechanisms of the three earthquakes from the China Earthquake Networks Center (CENC), U.S. Geological Survey (USGS), and Global Centroid Moment Tensor (Global CMT) are available at https://news.ceic.ac.cn/, https://earthquake.usgs.gov/, and https://www.globalcmt.org/, respectively. All websites were last accessed in November 2023. The supplemental material involves one table and one figure to support the discussion in the main article.

Declaration of Competing Interests

The authors acknowledge that there are no conflicts of interest recorded.

Acknowledgments

The authors thank Editor-in-Chief Allison Bent, reviewer Yifang Cheng, and other anonymous reviewers for their helpful comments that improved this article. The authors thank the European Space Agency (ESA) for their open data policy. This study is supported by the Strategic Priority Research Program of the Chinese Academy of Sciences (XDB 41000000), the National Natural Science Foundation of China (U2139203, 42104061, 41904007), the Natural Science Basic Research Program of Shaanxi (Program Number 2023-JC-QN-0292), the Fundamental Research Funds for the Central Universities, CHD (300102262512), Hong Kong Research Grant Council (Number 14303721), and the Knowledge Innovation Program of Wuhan-Shuguang Project.

References

Abbas, A., H. Yang, and J. Zi (2024). Deciphering the low-frequency seismic signals in the Weiyuan shale gas field: Implications for reservoir and structural heterogeneity, *Geophys. J. Int.* **237,** no. 1, 109–122.

Bagnardi, M., and A. Hooper (2018). Inversion of surface deformation data for rapid estimates of source parameters and uncertainties: A Bayesian approach, *Geochem. Geophys. Geosys.* **19,** no. 7, 2194–2211.

Bao, X., and D. W. Eaton (2016). Fault activation by hydraulic fracturing in western Canada, *Science* **354,** no. 6318, 1406–1409.

Chu, R., and M. Sheng (2023). Stress features inferred from induced earthquakes in the Weiyuan shale gas block in southwestern China, *J. Geophys. Res.* **128,** no. 2, doi: 10.1029/2022JB025344.

Costantini, M. (1998). A novel phase unwrapping method based on network programming, *IEEE Trans. Geosci. Remote* **36,** no. 3, 813–821.

Dai, K., Y. Zheng, R. Guo, and J. Xu (2023). Source characteristics of the mainshock and aftershocks of the 2019 Changning earthquake

sequence: Implications for fluid effects, *Sci. China Earth Sci.* **66,** doi: 10.1007/s11430-022-1040-4.

Deng, K., Y. Liu, and R. M. Harrington (2016). Poroelastic stress triggering of the December 2013 Crooked Lake, Alberta, induced seismicity sequence, *Geophys. Res. Lett.* **43,** no. 16, 8482–8491.

Dong, D., Z. Shi, Q. Guan, S. Jiang, M. Zhang, C. Zhang, S. Wang, S. Sun, R. Yu, D. Liu, *et al.* (2018). Progress, challenges and prospects of shale gas exploration in the Wufeng-Longmaxi reservoirs in the Sichuan basin, *Nat. Gas Indus. B* **5,** no. 5, 415–424.

Elliott, J. R., R. J. Walters, and T. J. Wright (2016). The role of space-based observation in understanding and responding to active tectonics and earthquakes, *Nat. Commun.* **7,** no. 1, 1–16.

Ellsworth, W. L. (2013). Injection-induced earthquakes, *Science* **341,** no. 6142, 1225942, doi: 10.1126/science.1225942.

Eyre, T. S., D. W. Eaton, D. I. Garagash, M. Zecevic, M. Venieri, R. Weir, and D. C. Lawton (2019). The role of aseismic slip in hydraulic fracturing-induced seismicity, *Sci. Adv.* **5,** no. 8, doi: 10.1126/sciadv.aav7172.

Eyre, T. S., S. Samsonov, W. Feng, H. Kao, and D. W. Eaton (2022). InSAR data reveal that the largest hydraulic fracturing-induced earthquake in Canada, to date, is a slow-slip event, *Sci. Rep.* **12,** no. 1, 2043, doi: 10.1038/s41598-022-06129-3.

Goebel, T. H. W., and E. E. Brodsky (2018). The spatial footprint of injection wells in a global compilation of induced earthquake sequences, *Science* **361,** no. 6405, 899–904.

Goldstein, R. M., and C. L. Werner (1998). Radar interferogram filtering for geophysical applications, *Geophys. Res. Lett.* **25,** no. 21, 4035–4038.

Guo, R., L. Li, W. Zhang, Y. Zhang, X. Tang, K. Dai, Y. Li, L. Zhang, and J. Wang (2023). Kinematic slip evolution during the 2022 M_s 6.8 Luding, China, earthquake: Compatible with the preseismic locked patch, *Geophys. Res. Lett.* **50,** no. 5, doi: 10.1029/2023GL103164.

Guo, R., Y. Zheng, and J. Xu (2020). Stress modulation of the seismic gap between the 2008 M_s 8.0 Wenchuan earthquake and the 2013 M_s 7.0 Lushan earthquake and implications for seismic hazard, *Geophys. J. Int.* **221,** no. 3, 2113–2125.

Hansen, P. C. (1999). The L-curve and its use in the numerical treatment of inverse problems, in *Computational Inverse Problems in Electrocardiology*, P. Johnston (Editor), WIT Press, Southampton, United Kingdom, 119–142.

Ji, L., Q. Wang, J. Xu, and J. Feng (2017). The 1996 M_w 6.6 Lijiang earthquake: Application of JERS-1 SAR interferometry on a typical normal-faulting event in the northwestern Yunnan rift zone, SW China, *J. Asian Earth Sci.* **146,** 221–232.

Jiang, G., Y. Wen, K. Li, L. Fang, C. Xu, Y. Zhang, and X. Xu (2018). A NE-trending oblique-slip fault responsible for the 2016 Zaduo earthquake (Qinghai, China) revealed by InSAR data, *Pure Appl. Geophys.* **175,** 4275–4288.

Kagan, Y. Y. (1991). 3-D rotation of double-couple earthquake sources, *Geophys. J. Int.* **106,** no. 3, 709–716.

Kozłowska, M., M. R. Brudzinski, P. Friberg, R. J. Skoumal, N. D. Baxter, and B. S. Currie (2018). Maturity of nearby faults influences seismic hazard from hydraulic fracturing, *Proc. Natl. Acad. Sci. Unit. States Am.* **115,** no. 8, E1720–E1729.

Lei, X., X. Li, Q. Li, S. Ma, B. Fu, and Y. Cui (2014). Role of immature faults in Injection-induced seismicity in oil/gas reservoirs–A case study of the Sichuan basin, China, *Seismol. Geol.* **36,** no. 3, 625–643.

Lei, X., J. Su, and Z. Wang (2020). Growing seismicity in the Sichuan basin and its association with industrial activities, *Sci. China Earth Sci.* **63,** 1633–1660.

Liu, G., R. Lu, D. He, W. Tao, P. Su, W. Zhang, J. Zhang, F. Xu, X. Sun, and W. Wang (2023). Detailed imaging of a seismogenic fault that potentially induced the two 2019 Weiyuan moderate earthquakes in the Sichuan basin, China, *Seismol. Soc. Am.* **94,** no. 3, 1379–1391.

Liu, N., and G. Wang (2016). Shale gas sweet spot identification and precise geo-steering drilling in Weiyuan block of Sichuan basin, SW China, *Pet. Explor. Dev.* **43,** no. 6, 1067–1075.

Liu, S., Y. Yang, B. Deng, Y. Zhong, L. Wen, W. Sun, Z. Li, L. Jansa, J. Li, J. Song, *et al.* (2021). Tectonic evolution of the Sichuan basin, southwest China, *Earth Sci. Rev.* **213,** 103470, doi: 10.1038/s41598-022-06129-3.

Luo, H., T. Wang, and S. Wei (2022). Systematic comparison of InSAR and seismic source models for moderate-size earthquakes in western china: Implication to the seismogenic capacity of the shallow crust, *J. Geophys. Res.* **127,** no. 10, doi: 10.1029/2022JB024794.

Massonnet, D., K. Feigl, M. Rossi, and F. Adragna (1994). Radar interferometric mapping of deformation in the year after the Landers earthquake, *Nature* **369,** no. 6477, 227–230.

Okada, Y. (1985). Surface deformation due to shear and tensile faults in a half-space, *Bull. Seismol. Soc. Am.* **75,** no. 4, 1135–1154.

Schultz, R., R. J. Skoumal, M. R. Brudzinski, D. Eaton, B. Baptie, and W. Ellsworth (2020). Hydraulic fracturing-induced seismicity, *Rev. Geophys.* **58,** no. 3, doi: 10.1029/2019RG000695.

Segall, P., and S. Lu (2015). Injection-induced seismicity: Poroelastic and earthquake nucleation effects, *J. Geophys. Res.* **120,** no. 7, 5082–5103.

Sheng, M., R. Chu, S. Ni, Y. Wang, L. Jiang, and H. Yang (2020). Source parameters of three moderate size earthquakes in Weiyuan, China, and their relations to shale gas hydraulic fracturing, *J. Geophys. Res.* **125,** no. 10, doi: 10.1029/2020JB019932.

Sheng, M., R. Chu, Z. Peng, Z. Wei, X. Zeng, Q. Wang, and Y. Wang (2022). Earthquakes triggered by fluid diffusion and boosted by fault reactivation in Weiyuan, China due to hydraulic fracturing, *J. Geophys. Res.* **127,** no. 5, doi: 10.1029/2021JB022963.

Tian, W., Q. Wu, K. Dai, R. Guo, Z. Yao, Z. Qiang, and F. Deng (2024). Seismological evidence for the existence of long-distance hydrological channel and its implication for fluid overpressure in southern Sichuan, China, *Geophys. Res. Lett.* **51,** doi: 10.1029/2023GL107167.

Verberne, B. A., C. He, and C. J. Spiers (2010). Frictional properties of sedimentary rocks and natural fault gouge from the Longmen Shan fault zone, Sichuan, China, *Bull. Seismol. Soc. Am.* **100,** no. 5B, 2767–2790.

Wang, M., and Z. K. Shen (2020). Present-day crustal deformation of continental China derived from GPS and its tectonic implications, *J. Geophys. Res.* **125,** no. 2, doi: 10.1029/2019JB018774.

Wang, M., J. Hubbard, A. Plesch, J. H. Shaw, and L. Wang (2016). Three-dimensional seismic velocity structure in the Sichuan basin, China, *J. Geophys. Res.* **121,** no. 2, 1007–1022.

Wang, M., H. Yang, L. Fang, L. Han, D. Jia, D. Jiang, and B. Yan (2020). Shallow faults reactivated by hydraulic fracturing: The 2019 Weiyuan earthquake sequences in Sichuan, China, *Seismol. Res. Lett.* **91,** no. 6, 3171–3181.

Wang, R., F. Diao, and A. Hoechner (2013). SDM-A geodetic inversion code incorporating with layered crust structure and curved fault geometry, *EGU General Assembly Conference Abstracts*, Vienna, Austria, 7–12 April 2013, EGU2013-2411.

Wang, S., G. Jiang, X. Lei, A.J. Barbour, X. Tan, C. Xu, and X. Xu (2022). Three $M_w \geq 4.7$ earthquakes within the Changning (China) shale gas field ruptured shallow faults intersecting with hydraulic fracturing wells, *J. Geophys. Res.* **127,** no. 2, doi: 10.1029/2021JB022946.

Wang, Y. M., J. L. Huang, S. F. Wang, D. Dong, C. Zhang, and Q. Guan (2016). Dissection of two calibrated areas of the Silurian Longmaxi Formation, Changning and Jiaoshiba, Sichuan basin, *Nat. Gas Geosci.* **27,** no. 3, 423–432.

Wei, G., G. Chen, S. Du, L. Zhang, and W. Yang (2008). Petroleum systems of the oldest gas field in China: Neoproterozoic gas pools in the Weiyuan gas field, Sichuan basin, *Mar. Petrol. Geol.* **25,** nos. 4/5, 371–386.

Werner, C., U. Wegmüller, T. Strozzi, and A. Wiesmann (2000). Gamma SAR and interferometric processing software, *Proc. of the ERS-ENVISAT Symposium*, Gothenburg, Sweden, 16–20 October 2000.

Wong, W. C. J., J. Zi, H. Yang, and J. Su (2021). Spatial-temporal evolution of injection-induced earthquakes in the Weiyuan area determined by machine-learning phase picker and waveform cross-correlation, *Earth Planet. Phys.* **5,** no. 6, 520–531.

Yagüe-Martínez, N., P. Prats-Iraola, F.R. Gonzalez, R. Brcic, R. Shau, D. Geudtner, M. Eineder, and R. Bamler (2016). Interferometric processing of sentinel-1 TOPS data, *IEEE Trans. Geosci. Remote Sens.* **4,** no. 54, 2220–2234.

Yang, H., P. Zhou, N. Fang, G. Zhu, W. Xu, J. Su, F. Meng, and R. Chu (2020). A shallow shock: The 25 February 2019 M_L 4.9 earthquake in the Weiyuan shale gas field in Sichuan, China, *Seismol. Soc. Am.* **91,** no. 6, 3182–3194.

Yi, G., F. Long, M. Liang, M. Zhao, and S. Wang (2020). Geometry and tectonic deformation of seismogenic structures in the Rongxian-Weiyuan-Zizhong region, Sichuan basin: Insights from focal mechanism solutions, *Chin. J. Geophys.* **63,** no. 9, 3275–3291.

Yu, C., Z. Li, N. T. Penna, and P. Crippa (2018). Generic atmospheric correction model for interferometric synthetic aperture radar observations, *J. Geophys. Res.* **123,** no. 10, 9202–9222.

Zhai, G., M. Shirzaei, and M. Manga (2021). Widespread deep seismicity in the Delaware basin, Texas, is mainly driven by shallow wastewater injection, *Proc. Natl. Acad. Sci. Unit. States Am.* **118,** no. 20, doi: 10.1073/pnas.2102338118.

Zhang, J., H. Yang, J. Zi, J. Su, and X. Chen (2024). An improved estimation of stress drop and its application on induced earthquakes in the Weiyuan shale gas field in China, *Geophys. J. Int.* **236,** no. 3, 1785–1803, doi: 10.1093/gji/ggae014.

Zhao, Y., G. Jiang, X. Lei, C. Xu, B. Zhao, and X. Qiao (2023). The 2021 M_s 6.0 Luxian (China) earthquake: Blind reverse-fault rupture in deep sedimentary formations likely induced by pressure perturbation from hydraulic fracturing, *Geophys. Res. Lett.* **50,** no. 7, doi: 10.1029/2023GL103209.

Zi, J., H. Yang, J. Su, and L. Chen (2023). Structural constraints of induced earthquakes in the Weiyuan shale gas field revealed by high-resolution body-wave tomography and earthquake relocation, *Tectonophysics* **864,** 230007, doi: 10.1016/j.tecto.2023.230007.

Zou, C., D. Dong, Y. Wang, X. Li, J. Huang, S. Wang, Q. Guan, C. Zhang, H. Wang, H. Liu, *et al.* (2015). Shale gas in China: Characteristics, challenges and prospects (I), *Pet. Explor. Dev.* **42,** 753–767.

Zou, C., Z. Yang, S. Sun, Q. Zhao, W. Bai, H. Liu, S. Pan, S. Wu, and Y. Yuan (2020). Exploring petroleum inside source kitchen: Shale oil and gas in Sichuan basin, *Sci. China Earth Sci.* **63,** 934–953.

Manuscript received 9 November 2023
Published online 11 October 2024